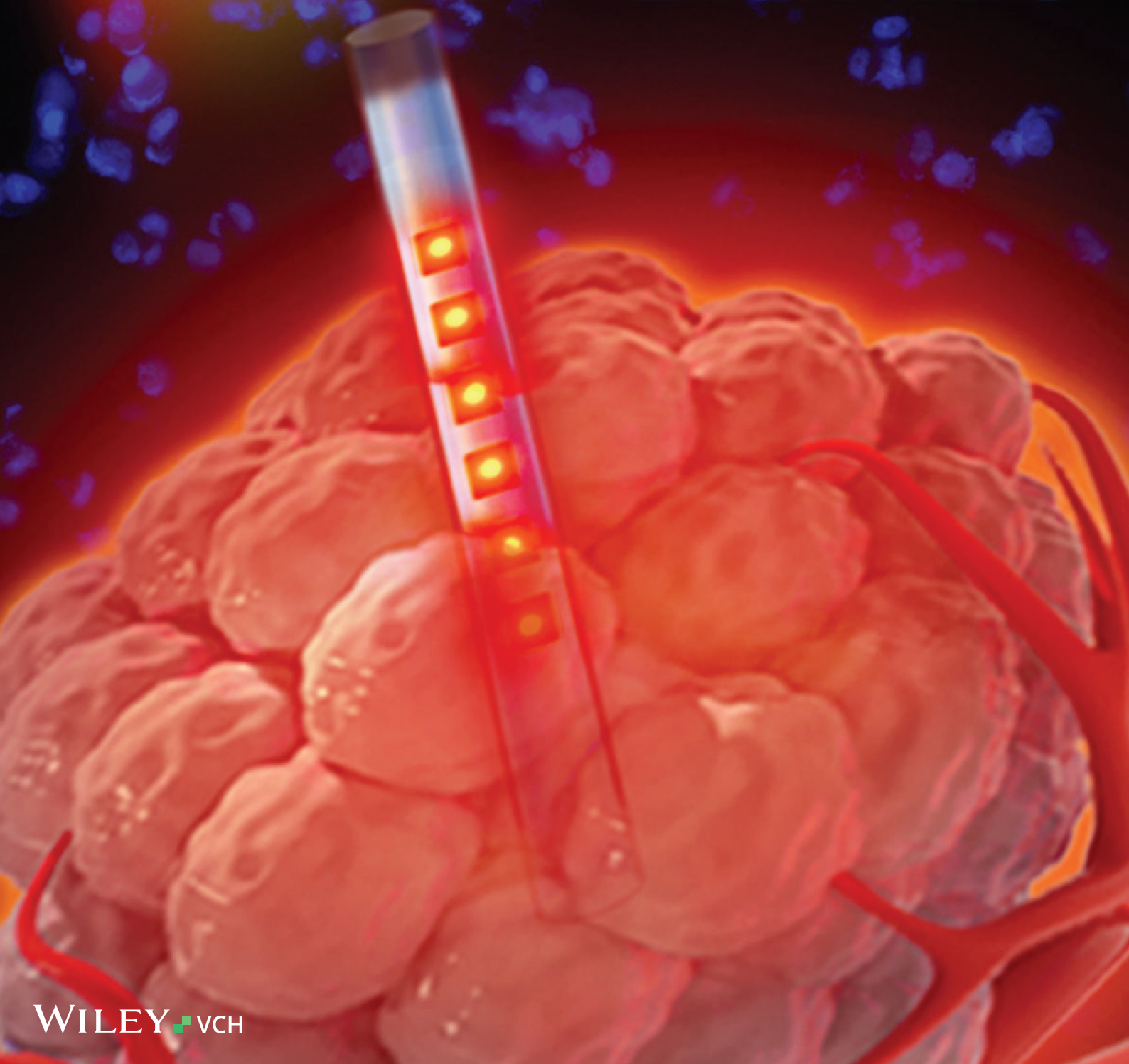


Vol. 11 • No. 19 • October 4 • 2023

www.advopticalmat.de

ADVANCED OPTICAL MATERIALS



Fully Implantable and Retrievable Upconversion Waveguides for Photodynamic Therapy in Deep Tissue

Zhao Shi, Xiaohan Gao, Xue Cai, Hongyou Zhao, Xiuhong Wang, Lingyun Zhao, Lan Yin, He Ding,* and Xing Sheng*

The clinical administration of biophotonic approaches, such as photodynamic therapy (PDT), is impeded by the low penetration of visible light in biological tissues. The cooperation of infrared (IR) light with deeper penetration and implantable IR-to-visible upconversion materials and devices establishes an effective strategy to generate visible light in deep tissue. In this work, a wirelessly powered upconversion waveguide-based light source is reported for PDT-based in vivo cancer treatments in deep tissue. Combining microscale IR-to-visible upconversion device arrays and a biocompatible waveguide, the implant exhibits enhanced IR transmission in biological environments and generates upconverted red emission in the target region at a depth >10 mm. The red illumination activates a photosensitizer in 5-aminolevulinic acid (5-ALA)-based PDT treatment, inducing massive apoptosis (>60% cell death) of tumor cells. After implanted in tumor-bearing mice, the waveguides enable chronic operation for more than two weeks and reveal ideal anti-tumor efficacies in the PDT process. Finally, the biocompatible waveguide can be retrieved from the tissue, leaving minimal traces after treatments. Such a waveguide implant represents a prospective technique to realize optical-based biological modulations and medical treatments within the body.

1. Introduction

In recent decades, photodynamic therapy (PDT) has been emerging as a promising approach to cancer treatment. Different from commonly adapted approaches like physical surgery, chemotherapy, and radiotherapy, PDT involves the cooperation of light, photosensitizers, and oxygen.^[1–5] Specifically activating photosensitizers by targeted illumination of required wavelengths (visible light in general) and then generating reactive oxygen species (ROS) in situ, PDT presents high selectivity against tumor cells, low invasiveness (compared to physical surgery), and less side effects (compared to chemo- and radiotherapies).^[6–11] In particular, PDT has been clinically applied for treating skin cancers or residual, exposed tumors after surgery, facilitated with external light sources.^[11–13] However, challenges remain for the use of PDT in deep biological tissues (more than a few

Z. Shi, X. Cai, X. Sheng
Department of Electronic Engineering
Beijing National Research Center for Information Science and Technology
Institute for Precision Medicine
Center for Flexible Electronics Technology
IDG/McGovern Institute for Brain Research
Tsinghua University
Beijing 100084, China
E-mail: xingsheng@tsinghua.edu.cn

X. Gao
Innovative Laboratory of Integrated Traditional Chinese and Western
Medicine for Brain Science (Disease)
School of Medicine
Tsinghua University
Beijing 100084, China

X. Gao
Department of Neurosurgery
Yuquan Hospital
School of Clinical Medicine
Tsinghua University
Beijing 100084, China

H. Zhao
Institute of Engineering Medicine
Beijing Institute of Technology
Beijing 100081, China

X. Wang
Laboratory for Biomedical Photonics
Institute of Laser Engineering
Faculty of Materials and Manufacturing
Beijing University of Technology
Beijing 100021, China

L. Zhao, L. Yin
School of Materials Science and Engineering
The Key Laboratory of Advanced Materials of Ministry of Education
State Key Laboratory of New Ceramics and Fine Processing
Center for Flexible Electronics Technology
Tsinghua University
Beijing 100084, China

H. Ding
Beijing Engineering Research Center of Mixed Reality and Advanced
Display
School of Optics and Photonics
Beijing Institute of Technology
Beijing 100081, China
E-mail: heding@bit.edu.cn

 The ORCID identification number(s) for the author(s) of this article can be found under <https://doi.org/10.1002/adom.202300689>

DOI: 10.1002/adom.202300689

millimeters underneath the skin), which usually own strong absorption and scattering in the visible and infrared (IR) ranges.^[14–16] To bypass this limit, implantable optical devices like microscale light-emitting diodes (LEDs), integrating with wireless power transfer systems, have been developed for deep-tissue light delivery in biomedicine.^[17–22]

Alternatively, IR light also serves as a viable supply for light delivery in tissue, leveraging the biological transparency window in the 700–1700 nm wavelength range.^[23–29] Upconversion materials and devices, which convert long-wavelength IR light into short-wavelength visible light,^[30–36] can utilize the transmitted IR illumination and produce visible emission, working as miniaturized implants in the deep tissue for biomodulation and sensing.^[37–43] Nevertheless, IR photons only extend the light penetration depth in tissues to a few millimeters, which still restrains the capability for deep-tissue light delivery.^[13–15] To overcome this issue, upconversion nanoparticles can be embedded into optical fibers, which promote the IR light delivery into deeper regions and also improve the stability of long-term applications.^[44] Likewise, the incorporation of high-performance optoelectronic devices^[45,46] and IR power supply vehicles system, in the form of light-guiding implants, can work as an in-body light source for PDT applications.

Here, we report an implantable IR-to-visible upconversion waveguide, which is constructed of a transparent flexible polymer slab and functionalized by embedded microscale optoelectronic devices, for in vivo PDT in deep tumors. Transdermally illuminated by external IR sources, the fully implanted waveguide facilitates light penetration into the tissue at depths of >10 mm. The contained microscale devices convert IR photons to visible ones and activate photosensitizers in the targeted tumor region. Designed to meet the requirements of practical PDT treatments, the waveguide has the following advantages. First, these miniaturized, lightweight implants can be fully implanted subcutaneously, without the need of tethering to external equipment or maintaining a window on the skin surface, thus reducing the risk of infection and minimizing the interference to animal behaviors. Second, the waveguide serves as a bridge between subdermal and deep tissues, effectively delivering IR photons to target sites. Third, the ideal biocompatibility and stability of the implant enable repeatable operations for long-term applications, and make it retrievable after treatment course. Experimentally, we implement these upconversion devices with the cooperation of 5-aminolevulinic acid (5-ALA) to inhibit the growth of cultured tumor cells (human brain glioma cells, U87MG, and mouse breast cancer cells, 4T1) in vitro and induce the regression of solid tumors (U87MG) in vivo by implanting them in living mice.

2. Results

2.1. Design and Operation of the Implantable Upconversion Waveguide

Figure 1a schematically illustrates the function of our developed implantable upconversion waveguide. Specifically, this wirelessly operated, fully implantable waveguide is subcutaneously implanted into the biological tissue and remotely activated by an external IR laser source at 810 nm. Near the bottom of the skin

tissue, the input end of the polymer waveguide receives the penetrated IR light, which is further transmitted into the deep site via the waveguide at a low loss. This waveguide design greatly enhances light propagation within the tissue and results in a high optical density in the deep region. The output end of the waveguide inserts into the targeted tumor region, and incorporates arrays of microscale devices that upconvert IR photons to visible ones, activating the photosensitizers to generate ROS for PDT. After the animal skin is sutured, the implanted upconversion waveguide is positioned within the subcutaneous tissue, without any tether on the skin surface and visible foreign objects protruding outside the skin.

The active components embedded in the output end of the polymer waveguide implant involve arrays of III–V semiconductor-based, microscale optoelectronic upconversion devices. Details of device design and fabrication are reported in our previous work.^[45] Briefly, such thin-film devices incorporate gallium arsenide (GaAs) photon diodes for IR absorption and indium gallium phosphide (InGaP) LEDs for red emission. These devices, with a size of $220 \times 220 \mu\text{m}^2$ and a thickness of $9 \mu\text{m}$, can be formed as a large-scale array on heterogeneous substrates with high yields, realizing efficient IR (810 nm) to red (630 nm) upconversion (Figure 1b). Transfer printing methods enable the integration of these thin-film emitters into a flexible waveguide made by an ultraviolet curable resin (Norland Optical Adhesive 65, NOA 65), with high transparency at 810 nm.^[47] NOA 65 has a refractive index of 1.524, which is larger than that of tissue (≈ 1.36) and helps confine IR light within the waveguide. Additionally, its low modulus ensures that the waveguide has mechanical properties matching those of biological tissues like skin and muscles. Figure 1c shows a typical design, including six upconversion devices on each side of the waveguide, with a Parylene C coating ($\approx 5 \mu\text{m}$) for waterproof and biocompatible encapsulation. The integrated waveguides have a diameter of $\approx 400 \mu\text{m}$ and a length that can be varied according to the depths of targeted tumors. Without the presence of any couplers, an external IR laser beam can be captured by the flexible waveguide and illuminate upconversion devices even if the waveguide is bent to angles up to 90° (Figure 1d).

2.2. Optical Properties of the Waveguide in Tissue

To verify the light-transport capability of the waveguide in the biological tissue, we carry out numerical simulations and experimental characterizations in **Figure 2**. In all cases, the waveguide structure (length = 10 mm and diameter = 0.5 mm) is fully implanted into the tissue with external IR illumination (810 nm) aligned to the input end, consistent with the condition shown in Figure 1a. In the model, rays of incident IR light (810 nm) or upconverted red light (630 nm) are traced by the Monte-Carlo method, to reveal the power distribution within the tissue (Figure 2a,b). Without the assistance of the waveguide, the optical intensity of the incident beam (810 nm) decays to 10% of the initial value at ≈ 4 mm depth due to the tissue absorption and scattering. By contrast, a substantial amount of IR photons can penetrate into the deep tissue (> 10 mm) via the waveguide implant (Figure 2a). At a depth of 11 mm underneath the skin, calculation results show that the optical density diminishes to $\approx 28\%$

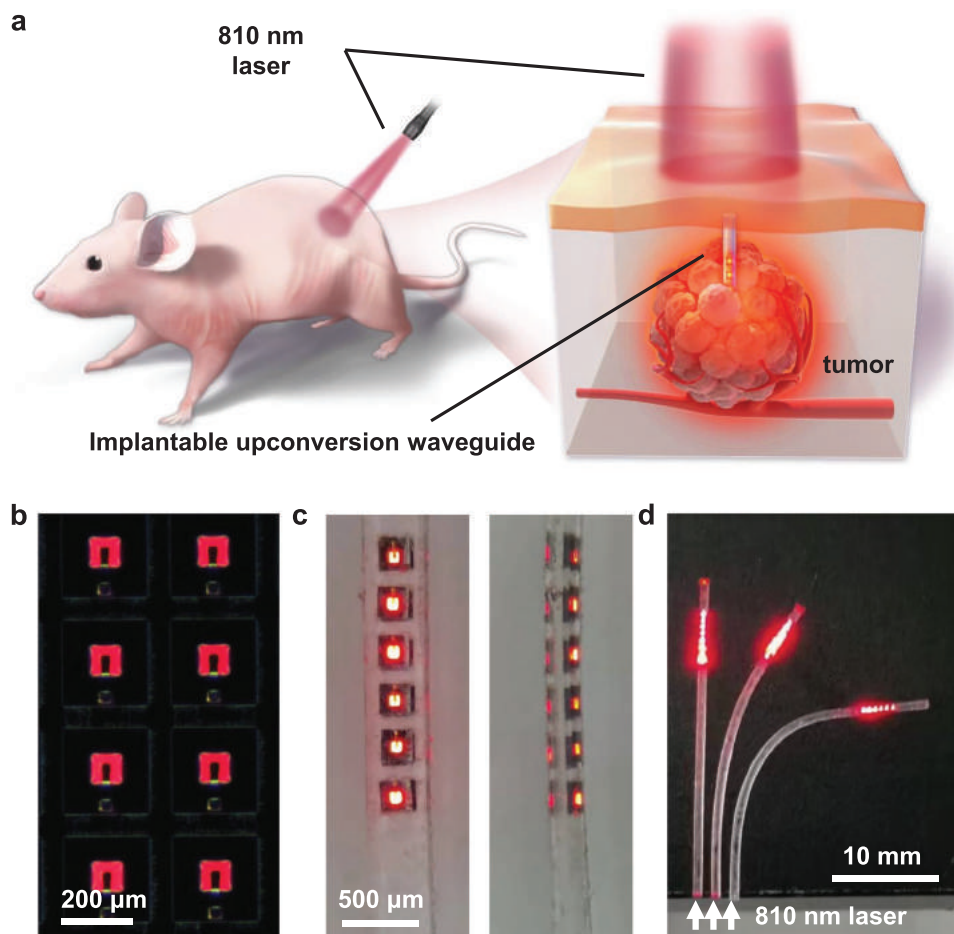


Figure 1. Implantable waveguide for IR-to-visible upconversion for PDT in the deep tissue. a) Scheme showing the PDT strategy by using an implantable waveguide incorporating microscale upconversion devices. The implantable waveguide facilitates the penetration of IR light (810 nm) into the deep tissue, then upconverts the IR light to visible light within the tumor. b) Optical microscope image showing an array of fabricated upconversion devices on GaAs under IR illumination. c) Photographs of a waveguide with multiple upconversion devices on both sides of the slab. Left: front view; Right: side view. d) Photographs showing flexible waveguides for IR light delivery and upconversion.

(with the waveguide) or 0.3% (without the waveguide) of the initial value. Furthermore, the IR propagation in the waveguide exhibits a relatively low loss, suggesting that the penetration depth of IR light mainly depends on the waveguide length. Near the output end of the waveguide, the upconverted red emission presents a nearly spherical distribution, due to the Lambertian emission nature of upconversion devices and the scattering caused by the biological tissue (Figure 2b). Detailed calculations show that, with an incident IR illumination of $\approx 500 \text{ mW cm}^{-2}$, the irradiance of red emission can reach $\approx 2.2 \text{ mW cm}^{-2}$ at a distance of $\approx 3 \text{ mm}$ from the upconversion emission source, resulting in an exposure dose of $\approx 4 \text{ J cm}^{-2}$ over $\approx 30 \text{ min}$, sufficient to activate most photosensitizers for PDT.^[13,17,48–51] Therefore, these device arrays can realize the effective treatment of a tumor with a diameter of up to $\approx 6 \text{ mm}$. Experimental characterizations performed in Figure 2c further verify numerical results. The setup involves a fabricated waveguide embedded in a synthetic tissue phantom, with the power density of IR illumination (810 nm) set to different values. Consistent with simulations, the distribution of red emission from upconversion devices covers a larger volume in

the tissue as the incident power increases. As a comparison, the red emission is much less prominent from the devices directly injected into the tissue (without the waveguide) under the same IR illumination. Clearly, the waveguide plays an important role in the light delivery into deep tissue.

To predict the thermal behaviors of the implant, temperature distributions within the tissue are investigated with numerical simulations, as well as in vivo tests. Supplied by IR illumination (810 nm) with a density of 500 mW cm^{-2} , temperature rises within the tissue are calculated by finite-element analysis. Maximum temperature rises occur near the surface skin tissue around the incident beam, reaching $\approx 0.6 \text{ }^\circ\text{C}$ above the normal body temperature (Figure S1a, Supporting Information). Animal tests are performed with a thermal camera capturing the skin temperature of a mouse under IR illumination (500 mW cm^{-2}). After $\approx 50 \text{ s}$ illumination, the maximum temperature stabilizes and reaches $\approx 2 \text{ }^\circ\text{C}$ above the normal skin temperature (Figure S1b,c, Supporting Information). Such photothermal effects are within the biological safety range and would have minimal influences on the animals.^[16,52]

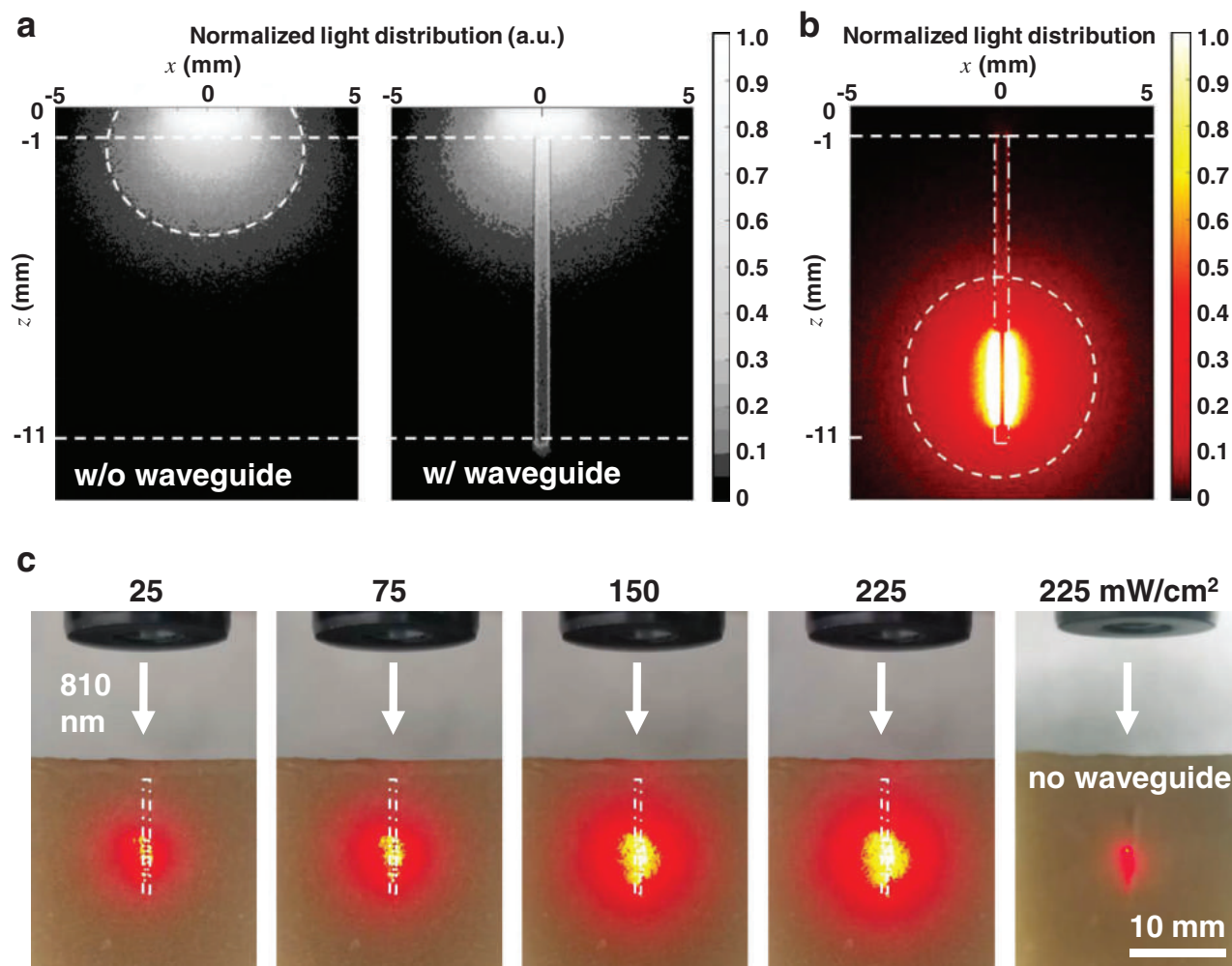


Figure 2. Numerical simulation and experimental characterization of the designed upconversion waveguide. a) Simulated power distribution within the biological tissue for IR light (810 nm) incident on the skin surface, with (right) and without (left) a waveguide (length = 10 mm) embedded in the biological tissue. Iso-intensity line (white dotted circle) shows 10% of the incident power density. b) Simulated power distribution in the biological tissue for red emission (630 nm) from the upconversion devices embedded in the waveguide. Iso-intensity line (white dotted circle) shows a red emission intensity of 2.2 mW cm^{-2} under IR illumination of 500 mW cm^{-2} . c) Experimental photographs illustrating red emissions from the upconversion devices embedded in the waveguide (length = 10 mm) implanted into a tissue phantom. The incident IR light is set to different power densities (columns 1–4: 25, 75, 150, and 225 mW cm^{-2}). The white dotted rectangle indicates the shape and the position of the waveguide. The result for upconversion devices directly embedded at a similar depth (without waveguide) is also presented for comparison in column 5 (incident IR power density = 225 mW cm^{-2}).

2.3. In Vitro Photodynamic Therapy (PDT) Results

To explore the performance of upconversion devices during the PDT process, we first carry out in vitro experiments on cultured tumor cells. We select 5-ALA, a clinically approved photosensitizer precursor, which can be metabolized into protoporphyrin IX (PpIX) in biological environments.^[53] 5-ALA presents high selectivity to tumor cells and causes preferential accumulation of PpIX in these cells.^[54–56] Especially, one of the activation peaks ($\approx 630 \text{ nm}$) in the absorption spectrum of PpIX exhibits a considerable overlap with the emission spectrum of our upconversion devices, but keeps away from the emission of the IR source at 810 nm (Figure 3a). In principle, the device can also be designed to target other absorption peaks of PpIX at shorter wavelengths (for example, 400 and 500 nm). However, the formation of infrared to blue or green upconversion devices requires the compacted

integration of InGaN blue LEDs and GaAs photodiodes, which are not lattice-matched and are more technically challenging. Figure 3b schematically illustrate the setup for cell experiments, in which an array of upconversion device is placed underneath a culture dish containing different types of tumor cells incubated with 5-ALA (U87MG or 4T1). Remotely illuminated by an IR laser beam (810 nm , 500 mW cm^{-2}), the device array provides irradiation at 630 nm to the cultured cells (Figure 3b, inset). Figure 3c,d compares cell viability testing results in different experimental conditions for U87MG and 4T1 cells, respectively. Each case involves five different experimental groups: i) control, 5-ALA (-), IR (-), device (-), ii) 5-ALA only, 5-ALA (+), IR (-), device (-), iii) 5-ALA + IR, 5-ALA (+), IR (+), device (-), iv) IR + device, 5-ALA (-), IR (+), device (+), and v) PDT, 5-ALA (+), IR (+), device (+). In both cases PDT-treated groups exhibit significant cell death in comparison to the control ones, with cell

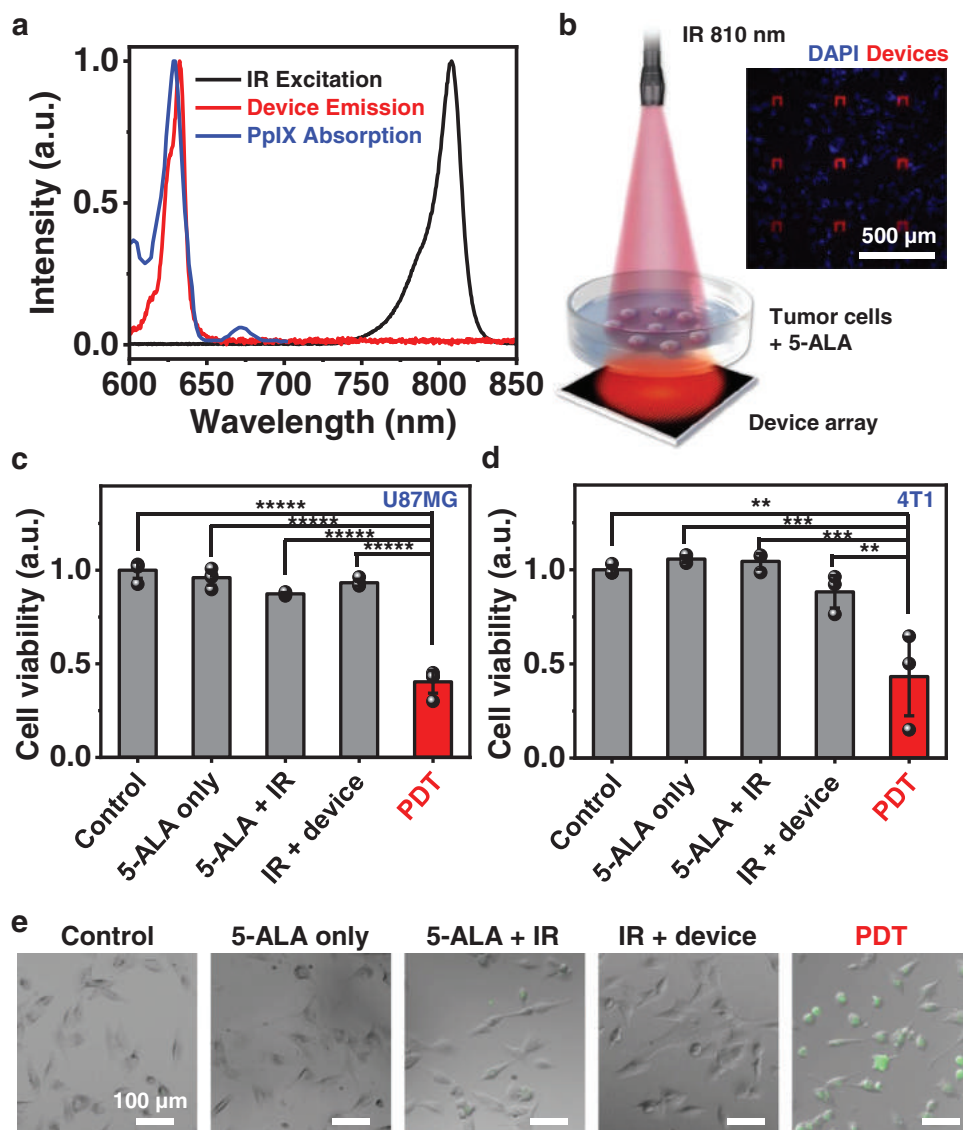


Figure 3. In vitro demonstration of PDT using the upconversion device array. a) Optical spectra for IR excitation (black), device emission (red), and PpIX absorption (blue). b) Schematic illustration of the experimental setup. Inset: Merged fluorescence image illustrating upconversion device array (red) and tumor cells (blue). DAPI (blue) indicates cell nuclei. Cell viability after PDT treatment for c) U87MG cells and d) 4T1 cells in different groups. The PDT groups indicate the results for cells applying both 5-ALA and IR light, with the device array on bottom (mean \pm s.d., $n = 3$ or 4 samples per group). Statistical analysis method is one-way repeated measures ANOVA for data. Sidak's multiple comparisons test, ** $p < 0.01$, *** $p < 0.001$, and **** $p < 0.00001$. e) Bright-field microscopic images showing cultured U87MG cells and reactive oxygen species (ROS) production in different groups. DCFH (green fluorescence) indicates the ROS production.

viability decreased to 40% for U87MG and 43% for 4T1 cells. Compared with the control group, measurements of cell viability show almost 60% death in PDT treatment group, in which the red illumination upconverted by IR light realized the activation of photosensitizer (Figure 3c). By contrast, neither the 5-ALA administration nor 5-ALA supplied with IR illumination can induce significant cell apoptosis, since the photosensitizers are not activated in these groups. Likewise, IR light on devices without 5-ALA does not directly kill the cells, either. The cell death can be attributed to ROS accumulation in cells treated by PDT, indicated by the fluorescence staining images in Figure 3e.

2.4. In Vivo PDT Results

After verifying the feasibility of photosensitizer activation by upconversion devices, we apply the implantable upconversion waveguide for tumor treatments in living animals (Figure 4). For in vivo PDT, we establish a tumor model by intracutaneously injecting U87MG cells in nude mice. Compared to the direct application of red illumination via an external light source, the implanted waveguide with embedded upconversion devices helps generate a more uniform light distribution within the tumor with a larger coverage, thus obtaining a more effective PDT process. After the tumor size reaches ≈ 5 mm diameter (≈ 10 days

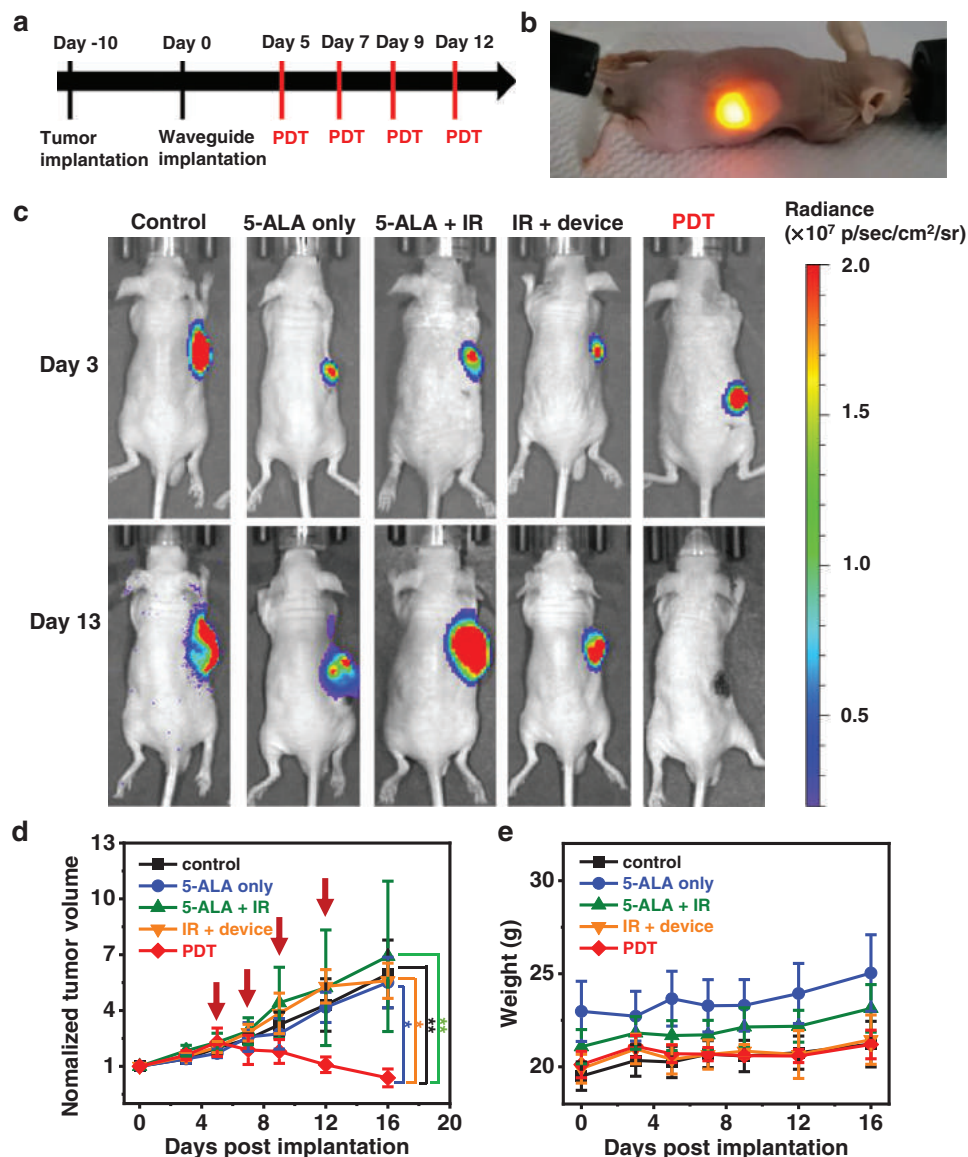


Figure 4. In vivo demonstration of PDT using upconversion waveguides. a) Protocol used for in vivo PDT, including tumor implantation, waveguide implantation, and PDT treatments. b) Photo of a nude mouse with the upconversion waveguide subcutaneously implanted in the tumor region, with devices emitting red light under IR illumination. c) Photos taken with an in vivo imaging system (IVIS), illustrating tumors before (day 3) and after PDT (day 13) for different groups. d) Measured tumor volumes (normalized) as a function of time after waveguide implantation for different groups. Red arrows indicate the day when applying PDT. e) Mouse weight change over the experiment. The statistical analysis of data uses one-way repeated measures ANOVA. Data show mean \pm s.d., $n = 5$ mice per group. Sidak's multiple comparisons test, * $p < 0.05$ and ** $p < 0.01$.

after tumor implantation), the waveguides are implanted subcutaneously at the tumor region, with the output end inserted into the tumor and the input end near the skin. Waiting for the recovery process of mice, PDT is performed on days 5, 7, 9, and 12 post-waveguide implantation along with the 5-ALA administration (Figure 4a). Under the IR illumination (810 nm, 500 mW cm⁻² in treatment) with an external source, the tumors are completely lighted up by red emission from upconversion devices, which can be distinctly visualized during the entire PDT course (Figure 4b).

The setup of experimental groups is similar to that of in vitro tests in Figure 3, and sham waveguides (without upconversion devices) are inserted into the mouse tumors for control, 5-ALA

only, and 5-ALA + IR groups. The tumor growth is monitored by in vivo fluorescence imaging systems (Figure 4c), as well as the direct geometry measurement (Figure 4d). On the first five days post-implantation, all the experimental groups present similar tumor growth states. Subsequently, multiple treatments in the PDT group significantly suppress the tumor growth, while tumors grow continuously in the other four groups. After 16 days, complete tumor regression occurs for some mice in the PDT group. Throughout the treatment period, all the mice present normal weight gain (Figure 4e). Histopathological examinations reveal microscopic views of the tissue, showing that remarkable cell apoptosis occurs in the tumor tissue for the PDT group, but

is almost invisible for other experimental groups (Figures S2–S4, Supporting Information). These results suggest that the PDT process effectively damages tumor cells and achieves the regression of tumors. In the other four groups, the cells reveal large nuclei, irregular shapes, and scanty cytoplasm, which are typical characteristics of tumor cells, while the cells in the PDT group present fractured geometries and constricted nuclei (Figure S3, Supporting Information). These results clearly demonstrate that the PDT effect induced by implantable upconversion waveguide performs desirable anti-tumor therapeutics, and exclude the possibility of chemotherapy-induced by photosensitizers or photothermal effects associated with the incident IR illumination.

The pathological sections gathered around the implantation position in the control group do not show obvious cell apoptosis or other adverse reactions (Figure S5, Supporting Information), indicating that encapsulated waveguides have ideal biocompatibility. Over the treatment process for more than two weeks, the implanted waveguides maintained their light-emitting functions (Figure S6, Supporting Information). Moreover, these waveguides can be retrieved and possibly employed for other experiments, further verifying their stability and biocompatibility.

3. Discussion

In summary, we develop an implantable active light-guiding device for PDT of tumors in the deep tissue, and demonstrate its capability in treating subdermal tumors *in vivo*. The fabricated waveguide can be fully implanted in the tissue without tethering outside, then transmit IR illumination efficiently and upconvert it into visible light, realizing a wireless approach to deep-tissue light delivery. Benefiting from the low-loss and high-index material, the subcutaneously implanted waveguide improves the transmission efficiency of IR light by several orders of magnitudes, bypassing the severe optical attenuation caused by biological environments. Furthermore, upconversion devices embedded into the waveguide offer sufficient doses of red emission for PDT. Other advantages of the waveguide include its stability during chronic operation and the possibility of reutilization after retrieval.

Although current proof-of-concept demonstrations are performed in the subcutaneous tissue *in vivo*, the waveguide design can be immediately adapted for PDT practice in the deep tissue, simply by increasing its length. The fabricated implant can be further optimized, by implementing upconversion devices with improved conversion efficiencies and different emission spectra for various photosensitizers.^[16,57] The waveguide geometry can also be varied, for example, to form a 3D structure with more distributed emission within the tumor region. In addition to PDT, the design can also be employed for other biomedical applications, such as photothermal therapy, fluorescence detection, and optogenetics.^[57–62] This implantable waveguide provides a generic strategy for wireless light delivery in biomedicine, specifically to combine the transmission and conversion of light by the integration of passive and active photonic devices.

4. Experimental Section

Fabrication of Upconversion Devices: Microscale optoelectronic upconversion devices were fabricated from the epitaxial structure on GaAs sub-

strates grown by metal-organic chemical vapor deposition (MOCVD). The epitaxial structure included the material layers of an indium gallium phosphide (InGaP)-based LED, a distributed Bragg reflector (DBR), a GaAs-based double-junction photodiode (PD), and an aluminum arsenide (AlAs) sacrificial layer. The geometric areas of LED and PD were defined by a photolithographic process and acid-based wet etching. Metallization was done by sputtering, following the deposition of an insulating layer made of UV-curable epoxy. After selectively removing the sacrificial layer in hydrofluoric acid (HF)-based solution, the devices could be picked up and transferred onto the foreign substrate using poly(dimethylsiloxane) (PDMS) stamps. The detailed process was described in the previous paper.^[45]

Fabrication of Implantable Waveguides: Norland Optical Adhesive 65 (NOA 65, Norland Products)^[47] served as the raw material for the implantable waveguide. NOA 65 formed thin films ($\approx 150\ \mu\text{m}$ thick) by casting or spin coating, and curing under UV illumination at 365 nm with a dose of $4.5\ \text{J cm}^{-2}$. The films were shaped into strips with a width of $\approx 400\ \mu\text{m}$ and varied lengths, by mechanical or laser milling. Epitaxially released, free-standing microscale upconversion devices were attached on one side or both sides of the NOA 65 films by the transfer-printing process.^[11] Another NOA 65 film was coated on the devices and cured again by UV light, forming cylindrically shaped waveguides. Finally, an encapsulation layer of Parylene C ($\approx 5\ \mu\text{m}$ thick) was deposited on the surface of waveguides by evaporation.

Optical Modeling and Calculation: Light distribution in biological tissue was simulated using the Monte-Carlo method by TracePro software.^[63] A cubic entity (edge length $> 20\ \text{mm}$) was set as biological tissue, with a cylindrical waveguide (diameter = 0.5 mm and length = 10 mm) embedded, with the input end close to the surface (distance = 1 mm). An 810 nm light beam (3 mm diameter) was placed on the selected surface of the tissue, aligned to the waveguide, and two 630 nm light source (rectangle with 3 mm length and 0.1 mm width) was placed in the emitting end of the waveguide with opposite orientation. The parameters used in the simulation are listed in Table S1 (Supporting Information). The irradiance of red emission at a certain position in biological tissue, could be calculated as $I_{\text{Red}} = I_{\text{IR}} \cdot \eta_{\text{IR}} \cdot \eta_{\text{Device}} \cdot \eta_{\text{Red}}$, where I_{IR} is the initial intensity of incident IR illumination ($500\ \text{mW cm}^{-2}$), η_{IR} is the efficiency of the IR transmittance at the location of upconversion devices, η_{Red} is the ratio of I_{Red} to the initial red emission from devices, and η_{Device} is related to the device upconversion efficiency. Based on the ray-tracing simulation results, $\eta_{\text{IR}} = 28.3\%$, and $\eta_{\text{Red}} = 10\%$ at the position of iso-intensity line in Figure 2b. Considering active areas and the quantum efficiency of the upconversion devices,^[11] η_{Device} could be determined to be 15.4%. Ultimately, the irradiance of red emission at the position of the iso-intensity line in Figure 2b was determined to be $\approx 2.2\ \text{mW cm}^{-2}$.

Light-Guiding Display: The synthetic tissue phantom that exhibits similar absorption and scattering properties to those of living tissues, was prepared to display the light propagation behaviors of the waveguide in biological environments (Figure 2c). Briefly, the synthetic tissue phantom was made of agarose (0.5% w/v), bovine hemoglobin blood (0.25% w/v), and intralipid (5% w/v) dissolved in a phosphate buffer solution (pH 7.4). Subsequently, the solution was blended, boiled, and naturally cooled to room temperature to form a gel. An upconversion waveguide (length = 10 mm) was embedded in the slab, parallel to the surface with a distance of 2 mm for observation. Encapsulated upconversion devices were embedded at the same position for the case without the waveguide. An IR laser beam (810 nm) with varied intensities was aligned to the input end of the waveguide. The light distribution of upconverted emission was shown on the surface of tissue phantom, and recorded by a camera with a bandpass filter (passing band 400–700 nm).

Thermal Modeling: The temperature distribution within the tissue was simulated by finite element analysis using COMSOL Multiphysics software.^[64] The coupling of two modules, “Radiation in Absorbing-Scattering Media” and “Biological Heat Transfer”, were employed in the software. A cylindrical entity (dimensions $> 20\ \text{mm}$) was set as biological tissue, with a surface layer (thickness = 1 mm) as the skin. An 810 nm light source (diameter = 5 mm, intensity = $500\ \text{mW cm}^{-2}$) was placed on the surface of the skin model. Considering the heat

dissipation, convection and radiation were set on the surface. The parameters of simulation are listed in Tables S2 and S3 (Supporting Information).

Temperature Measurements: Live mice (BALB/c Nude, Charles River) were used to test the temperature rise caused by IR irradiation. The awake mice were temporarily immobilized, and the IR laser (810 nm, 500 mW cm⁻²) was shone on the back of the mice. Thermography and temperature change over time were recorded using an infrared thermal imager (FOTRIC 220).

In Vitro PDT for Tumor Cells: In the experiments, upconversion device arrays were used to provide light illumination for tumor cells, which were incubated with 5-ALA (MedChemExpress). First, tumor cells (U87MG or 4T1) were cultured in 96-well plates (Corning) for 5 × 10³ per well, then were placed in the incubator (37 °C, 24 h) for adherent growth. Next, 5-ALA (in the basal culture medium) was added, with a final concentration of 2 mM. After 4 h, the medium was replaced by complete culture medium and PDT was carried out. Device arrays were placed underneath the culture dishes, and illuminated remotely by an 810 nm laser (500 mW cm⁻², 20 min). After another 24 h in the incubator, cell viability was determined using the Cell Counting Kit-8 (CCK-8) assay, and the absorbance was measured at 450 nm by a microplate reader.

ROS Imaging: ROS production was detected using 2',7'-Dichlorodihydrofluorescein diacetate (DCFH-DA, MedChemExpress). During the cell culture process, the DCFH-DA probe (20 μM in basal culture medium) was added in the plate, and incubated with tumor cells for 30 min, before the PDT was executed. After the illumination process, ROS production was visualized (488/525 ex/em) using a confocal fluorescence microscope (FV3000, Olympus).

Animal Preparation: Animal care and all experiments were in accordance with the institutional guidelines of Tsinghua University, with protocols proved by Institutional Animal Care and Use Committee (IACUC). All animals were socially housed in a 14/10 h (7 am–9 pm) light/dark cycle, with food and water *ad libitum*. Male BALB/c Nude mice (Charles River) aged at 4 weeks were used to prepare tumor models, by intracutaneous injection of U87MG cells (3 × 10⁶ per 100 μL) on the right side back. It was noted that the tumor location may change during the growth, since the injected tumor cells were unfixed before the solid tumor was completely formed. About 10 days after inoculation, the tumors of mice grew to ≈5 mm in diameter, and the mice were divided into five groups (*n* = 5 per group), according to the given grouping manner.

In Vivo PDT for Solid Tumors: All the mice were implanted with waveguides (sham devices for groups 1, 2, and 3; functional devices for groups 4 and 5) at the tumor site, by dermabrasion operation. The emitting end of the waveguide was inserted into the central position of tumor, and the input end was placed against the skin. After closing the wound, mice were given analgesic (meloxicam) for three consecutive days, then waiting for the recovery. PDT began on day 5 post implantation, and repeated on days 7, 9, and 12. Prior to IR illumination, mice were intraperitoneally injected with 200 mg kg⁻¹ 5-ALA. Four hours later, the tumor sites were given irradiated by an IR laser beam (810 nm, diameter 3 mm, 500 mW cm⁻², 30 min). During the PDT, mice were mildly anesthetized with isoflurane using a gas anesthesia machine (RWD). The measurements of tumor volumes and mouse weights were taken every two days. On day 18 post waveguide implantation, the tumors in uncured mice were removed to prevent reaching ethics limits or ulcerating, and kept in 10% formalin at 4 °C.

In Vivo Imaging System (IVIS) Imaging: Whole body imaging of mice was carried out on days 3 and 13, using an IVIS imager. Twenty minutes prior to imaging, mice were injected with a fluorescent dye solution (D-Luciferin potassium salt, Beyotime, with a concentration of 150 mg kg⁻¹). When anesthetized in the chamber, mice were imaged by detecting bioluminescence from the dye.

Histopathological Examination: The tumors were fixed in 10% formalin, dehydrated, embedded in paraffin, and sliced into 4 μm-thick sections using a Leica RM2016 slicer. The tumor slices were stained with hematoxylin and eosin (H&E), DAB TUNEL, and IF TUNEL, respectively, according to standard procedures, and photographed with an optical microscope (Nikon, Eclipse CI) and recorded by a digital camera (Nikon, DS-U3).

Supporting Information

Supporting Information is available from the Wiley Online Library or from the author.

Acknowledgements

Z.S. and X.G. contributed equally to this work. This work was supported by the National Natural Science Foundation of China (NSFC) (52272277 to X.S. and 62005016 to H.D.), Beijing Municipal Natural Science Foundation (Z220015 to L.Y.), China Postdoctoral Science Foundation (2021M701822 to X.G.), and Tsinghua Precise Medicine Foundation (100020102 to X.G.).

Conflict of Interest

The authors declare no conflict of interest.

Data Availability Statement

The data that support the findings of this study are available from the corresponding author upon reasonable request.

Keywords

biological waveguides, implantable, photodynamic therapy, upconversion

Received: March 22, 2023

Revised: July 27, 2023

Published online: August 17, 2023

- [1] D. Deda, K. Araki, *J. Braz. Chem. Soc.* **2015**, *26*, 2448.
- [2] D. E. J. G. J. Dolmans, D. Fukumura, R. K. Jain, *Nat. Rev. Cancer* **2003**, *3*, 380.
- [3] P. Agostinis, K. Berg, K. A. Cengel, T. H. Foster, A. W. Girotti, S. O. Gollnick, S. M. Hahn, M. R. Hamblin, A. Juzeniene, D. Kessel, M. Korbelik, J. Moan, P. Mroz, D. Nowis, J. Piette, B. C. Wilson, J. Golab, *Ca-Cancer J. Clin.* **2011**, *61*, 250.
- [4] M. M. Kim, A. Darafsheh, *Photochem. Photobiol.* **2020**, *96*, 280.
- [5] S. S. Lucky, K. C. Soo, Y. Zhang, *Chem. Rev.* **2015**, *115*, 1990.
- [6] B. C. Wilson, M. S. Patterson, *Phys. Med. Biol.* **2008**, *53*, R61.
- [7] J. T. Ping, H. S. Peng, W. B. Duan, F. T. You, M. Song, Y. Q. Wang, *J. Mater. Chem. B* **2016**, *4*, 4482.
- [8] C. Wang, L. Cheng, Z. Liu, *Theranostics* **2013**, *3*, 317.
- [9] J. Moan, *J. Photochem. Photobiol., B* **1990**, *5*, 521.
- [10] R. R. Allison, C. H. Sibata, *Photodiagn. Photodyn. Ther.* **2010**, *7*, 61.
- [11] K. Plaetzer, B. Krammer, J. Berlanda, F. Berr, T. Kiesslich, *Lasers Med. Sci.* **2009**, *24*, 259.
- [12] C. Sawyers, *Nature* **2004**, *432*, 294.
- [13] S. H. Yun, S. J. J. Kwok, *Nat. Biomed. Eng.* **2017**, *1*, 0008.
- [14] T. S. Mang, *Photodiagn. Photodyn. Ther.* **2004**, *1*, 43.
- [15] G.-H. Lee, H. Moon, H. Kim, G. H. Lee, W. Kwon, S. Yoo, D. Myung, S. H. Yun, Z. Bao, S. K. Hahn, *Nat. Rev. Mater.* **2020**, *5*, 149.
- [16] N. M. Idris, M. K. Gnanasamandhan, J. Zhang, P. C. Ho, R. Mahendran, Y. Zhang, *Nat. Med.* **2012**, *18*, 1580.
- [17] A. Bansal, F. Yang, T. Xi, Y. Zhang, J. S. Ho, *Proc. Natl. Acad. Sci. USA* **2018**, *115*, 1469.
- [18] K. Yamagishi, I. Kirino, I. Takahashi, H. Amano, S. Takeoka, Y. Morimoto, T. Fujie, *Nat. Biomed. Eng.* **2019**, *3*, 27.

- [19] I. Kirino, K. Fujita, K. Sakanoue, R. Sugita, K. Yamagishi, S. Takeoka, T. Fujie, S. Uemoto, Y. Morimoto, *Sci. Rep.* **2020**, *10*, 22017.
- [20] A. Kim, J. Zhou, S. Samaddar, S. H. Song, B. D. Elzey, D. H. Thompson, B. Ziaie, *Sci. Rep.* **2019**, *9*, 1395.
- [21] Z. Liu, L. Xu, Q. Zheng, Y. Kang, B. Shi, D. Jiang, H. Li, X. Qu, Y. Fan, Z. L. Wang, Z. Li, *ACS Nano* **2020**, *14*, 8074.
- [22] H.-J. Kim, W. Sritandi, Z. Xiong, J. S. Ho, *Biophys. Rev.* **2023**, *4*, 011304.
- [23] A. W. Sainter, T. A. King, M. R. Dickinson, *J. Biomed. Opt.* **2004**, *9*, 193.
- [24] F. Yang, Q. Zhang, S. Huang, D. Ma, *J. Mater. Chem. B* **2020**, *8*, 7856.
- [25] E. Hemmer, A. Benayas, F. Légaré, F. Vetrone, *Nanoscale Horiz.* **2016**, *1*, 168.
- [26] Y. Chen, S. Wang, F. Zhang, *Nat. Rev. Bioeng.* **2023**, *1*, 60.
- [27] M. Zhao, A. Sik, H. Zhang, F. Zhang, *Adv. Opt. Mater.* **2022**, *11*, 2202039.
- [28] Q. Ju, X. Chen, F. Ai, D. Peng, X. Lin, W. Kong, P. Shi, G. Zhu, F. Wang, *J. Mater. Chem. B* **2015**, *3*, 3548.
- [29] J. Kim, J. Seo, D. Jung, T. Lee, H. Ju, J. Han, N. Kim, J. Jeong, S. Cho, J. H. Seol, J. Lee, *Proc. Natl. Acad. Sci. USA* **2020**, *117*, 16856.
- [30] F. Auzel, *Chem. Rev.* **2004**, *104*, 139.
- [31] X. Liu, C. H. Yan, J. A. Capobianco, *Chem. Soc. Rev.* **2015**, *44*, 1299.
- [32] J. Zhou, Q. Liu, W. Feng, Y. Sun, F. Li, *Chem. Rev.* **2015**, *115*, 395.
- [33] H. Dong, L.-D. Sun, C.-H. Yan, *J. Am. Chem. Soc.* **2021**, *143*, 20546.
- [34] H. Dong, L.-D. Sun, C.-H. Yan, *Chem. Soc. Rev.* **2015**, *44*, 1608.
- [35] P. Qi, Y. Dai, Y. Luo, G. Tao, L. Zheng, D. Liu, T. Zhang, J. Zhou, B. Shen, F. Lin, Z. Liu, Z. Fang, *Light: Sci. Appl.* **2022**, *11*, 176.
- [36] X. Guo, Y. Liu, Q. Chen, D. Zhao, Y. Ma, *Adv. Opt. Mater.* **2018**, *6*, 1700981.
- [37] B. Zhou, B. Shi, D. Jin, X. Liu, *Nat. Nanotechnol.* **2015**, *10*, 924.
- [38] M. Wu, D. N. Congreve, M. W. B. Wilson, J. Jean, N. Geva, M. Welborn, T. Van Voorhis, V. Bulović, M. G. Bawendi, M. A. Baldo, *Nat. Photonics* **2015**, *10*, 31.
- [39] Z. Deutsch, L. Neeman, D. Oron, *Nat. Nanotechnol.* **2013**, *8*, 649.
- [40] A. Teitelboim, D. Oron, *ACS Nano* **2016**, *10*, 446.
- [41] L. Hu, P. Wang, M. Zhao, L. Liu, L. Zhou, B. Li, F. H. Albaqami, A. M. El-Toni, X. Li, Y. Xie, X. Sun, F. Zhang, *Biomaterials* **2018**, *163*, 154.
- [42] Y. Wang, X. Lin, X. Chen, X. Chen, Z. Xu, W. Zhang, Q. Liao, X. Duan, X. Wang, M. Liu, F. Wang, J. He, P. Shi, *Biomaterials* **2017**, *142*, 136.
- [43] X. Lin, X. Chen, W. Zhang, T. Sun, P. Fang, Q. Liao, X. Chen, J. He, M. Liu, F. Wang, P. Shi, *Nano Lett.* **2018**, *18*, 948.
- [44] D. B. L. Teh, A. Bansal, C. Chai, T. B. Toh, R. A. J. Tucker, G. G. L. Gammad, Y. Yeo, Z. Lei, X. Zheng, F. Yang, J. S. Ho, N. Boleyn, B. C. Wu, M. K. Gnanasamandhan, L. Hooi, G. S. Dawe, C. Libedinsky, W.-Y. Ong, B. Halliwell, E. K.-H. Chow, K.-L. Lim, Y. Zhang, B. K. Kennedy, *Adv. Mater.* **2020**, *32*, 2001459.
- [45] H. Ding, L. Lu, Z. Shi, D. Wang, L. Li, X. Li, Y. Ren, C. Liu, D. Cheng, H. Kim, N. C. Giebink, X. Wang, L. Yin, L. Zhao, M. Luo, X. Sheng, *Proc. Natl. Acad. Sci. USA* **2018**, *115*, 6632.
- [46] H. Ding, G. Lv, X. Cai, J. Chen, Z. Cheng, Y. Peng, G. Tang, Z. Shi, Y. Xie, X. Fu, L. Yin, J. Yang, Y. Wang, X. Sheng, *Light: Sci. Appl.* **2022**, *11*, 130.
- [47] <http://www.norlandprod.com/adhesives/noa%2065.html> (accessed: August 2023).
- [48] R. Bachor, C. R. Shea, R. Gillies, T. Hasan, *Proc. Natl. Acad. Sci. USA* **1991**, *88*, 1580.
- [49] X. Shi, H. Zhang, W. Jin, W. Liu, H. Yin, Y. Li, H. Dong, *J. Photochem. Photobiol., B* **2019**, *198*, 111586.
- [50] K. Mahmoudi, K. L. Garvey, A. Bouras, G. Cramer, H. Stepp, J. G. Jesu Raj, D. Bozec, T. M. Busch, C. G. Hadjipanayis, *J. Neuro-Oncol.* **2019**, *141*, 595.
- [51] M. S. Mathews, E. Angell-Petersen, R. Sanchez, C.-H. Sun, V. Vo, H. Hirschberg, S. J. Madsen, *Lasers Surg. Med.* **2009**, *41*, 578.
- [52] A. Bozkurt, B. Onaral, *Biomed. Eng.* **2004**, *3*, 9.
- [53] P. Babilas, S. Schreml, M. Landthaler, R. M. Szeimies, *Photodermatol., Photoimmunol. Photomed.* **2010**, *26*, 118.
- [54] W. Stummer, U. Pichlmeier, T. Meinel, O. D. Wiestler, F. Zanella, H.-J. Reulen, *Lancet Oncol.* **2006**, *7*, 392.
- [55] H. Stepp, W. Stummer, *Lasers Surg. Med.* **2018**, *50*, 399.
- [56] K. McNicholas, M. N. MacGregor, J. M. Gleadle, *Br. J. Cancer* **2019**, *121*, 631.
- [57] L. Li, L. Lu, Y. Ren, G. Tang, Y. Zhao, X. Cai, Z. Shi, H. Ding, C. Liu, D. Cheng, Y. Xie, H. Wang, X. Fu, L. Yin, M. Luo, X. Sheng, *Nat. Commun.* **2022**, *13*, 839.
- [58] T.-I. Kim, J. G. McCall, Y. H. Jung, X. Huang, E. R. Siuda, Y. Li, J. Song, Y. M. Song, H. A. Pao, R.-H. Kim, C. Lu, S. D. Lee, I.-S. Song, G. Shin, R. Al-Hasani, S. Kim, M. P. Tan, Y. Huang, F. G. Omenetto, J. A. Rogers, M. R. Bruchas, *Science* **2013**, *340*, 211.
- [59] A. Burton, S. N. Obaid, A. Vázquez-Guardado, M. B. Schmit, T. Stuart, L. Cai, Z. Chen, I. Kandela, C. R. Haney, E. A. Waters, H. Cai, J. A. Rogers, L. Lu, P. Gutruf, *Proc. Natl. Acad. Sci.* **2020**, *117*, 2835.
- [60] H. Arami, S. Kananian, L. Khalifehzadeh, C. B. Patel, E. Chang, Y. Tanabe, Y. Zeng, S. J. Madsen, M. J. Mandella, A. Natarajan, E. E. Peterson, R. Sinclair, A. S. Y. Poon, S. S. Gambhir, *Nat. Nanotechnol.* **2022**, *17*, 1015.
- [61] H. Zhou, X. Zeng, A. Li, W. Zhou, L. Tang, W. Hu, Q. Fan, X. Meng, H. Deng, L. Duan, Y. Li, Z. Deng, X. Hong, Y. Xiao, *Nat. Commun.* **2020**, *11*, 6183.
- [62] L. Lu, Z. Yang, K. Meacham, C. Cvetkovic, E. A. Corbin, A. Vázquez-Guardado, M. Xue, L. Yin, J. Boroumand, G. Pakeltis, T. Sang, K. J. Yu, D. Chanda, R. Bashir, R. W. Gereau IV, X. Sheng, J. A. Rogers, *Adv. Energy Mater.* **2018**, *8*, 1703035.
- [63] <https://lambdare.com/tracepro>, (accessed: August 2023)
- [64] <https://www.comsol.com>, (accessed: August 2023)

ADVANCED OPTICAL MATERIALS

Supporting Information

for *Adv. Optical Mater.*, DOI 10.1002/adom.202300689

Fully Implantable and Retrievable Upconversion Waveguides for Photodynamic Therapy in Deep Tissue

Zhao Shi, Xiaohan Gao, Xue Cai, Hongyou Zhao, Xiuhong Wang, Lingyun Zhao, Lan Yin, He Ding and Xing Sheng**

Supporting Information

**Fully Implantable and Retrievable Upconversion Waveguides for Photodynamic
Therapy in Deep Tissue**

*Zhao Shi, Xiaohan Gao, Xue Cai, Hongyou Zhao, Xiuhong Wang, Lingyun Zhao, Lan Yin, He
Ding*, Xing Sheng**

Figure S1

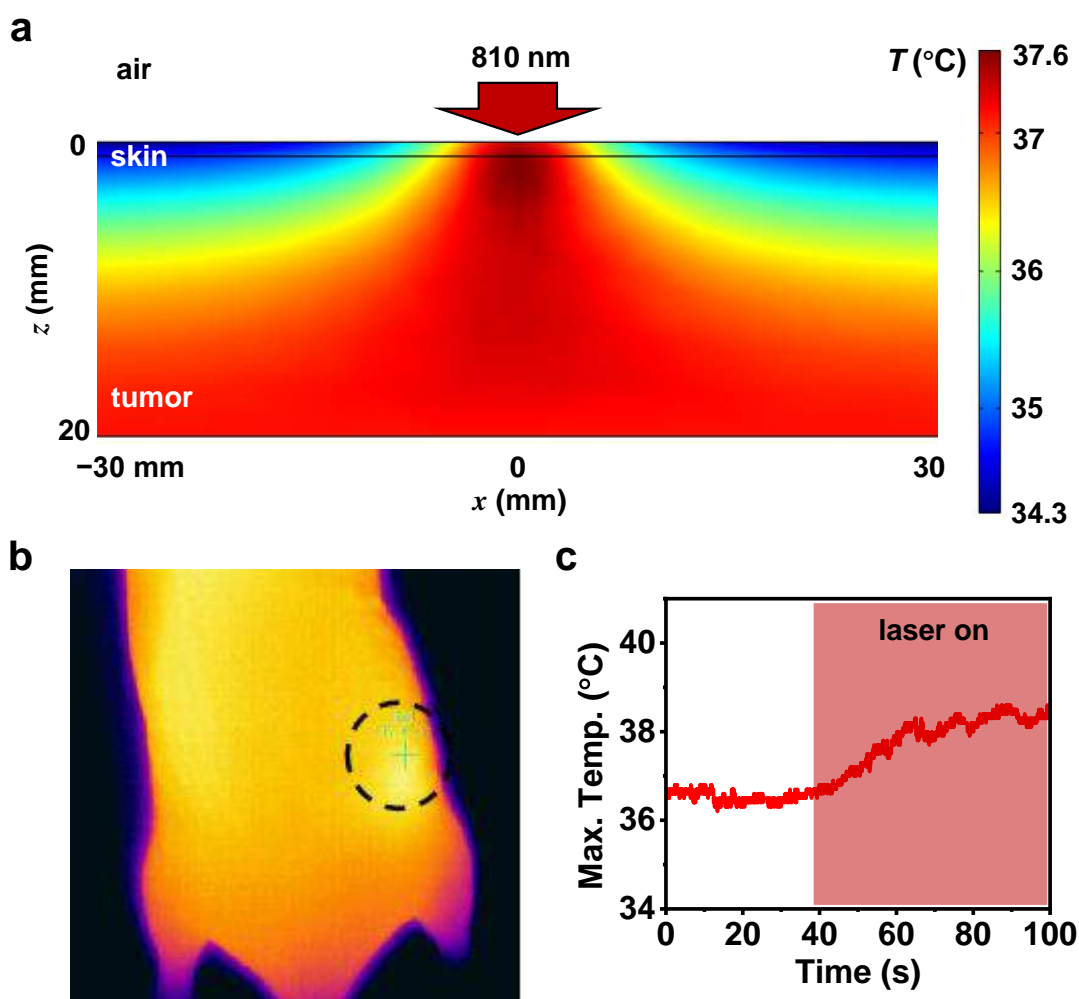


Figure S1. Photothermal effects of the IR excitation source. (a) Simulated temperature distribution within tissue around the incident position of IR light (power density = 500 mW/cm²). (b) Thermography of a living mouse under the IR illumination. Measured maximum temperature is 38.4 °C. White dotted circle indicates the incident laser spot. (c) Measured maximum temperature as a function of illumination time.

Figure S2

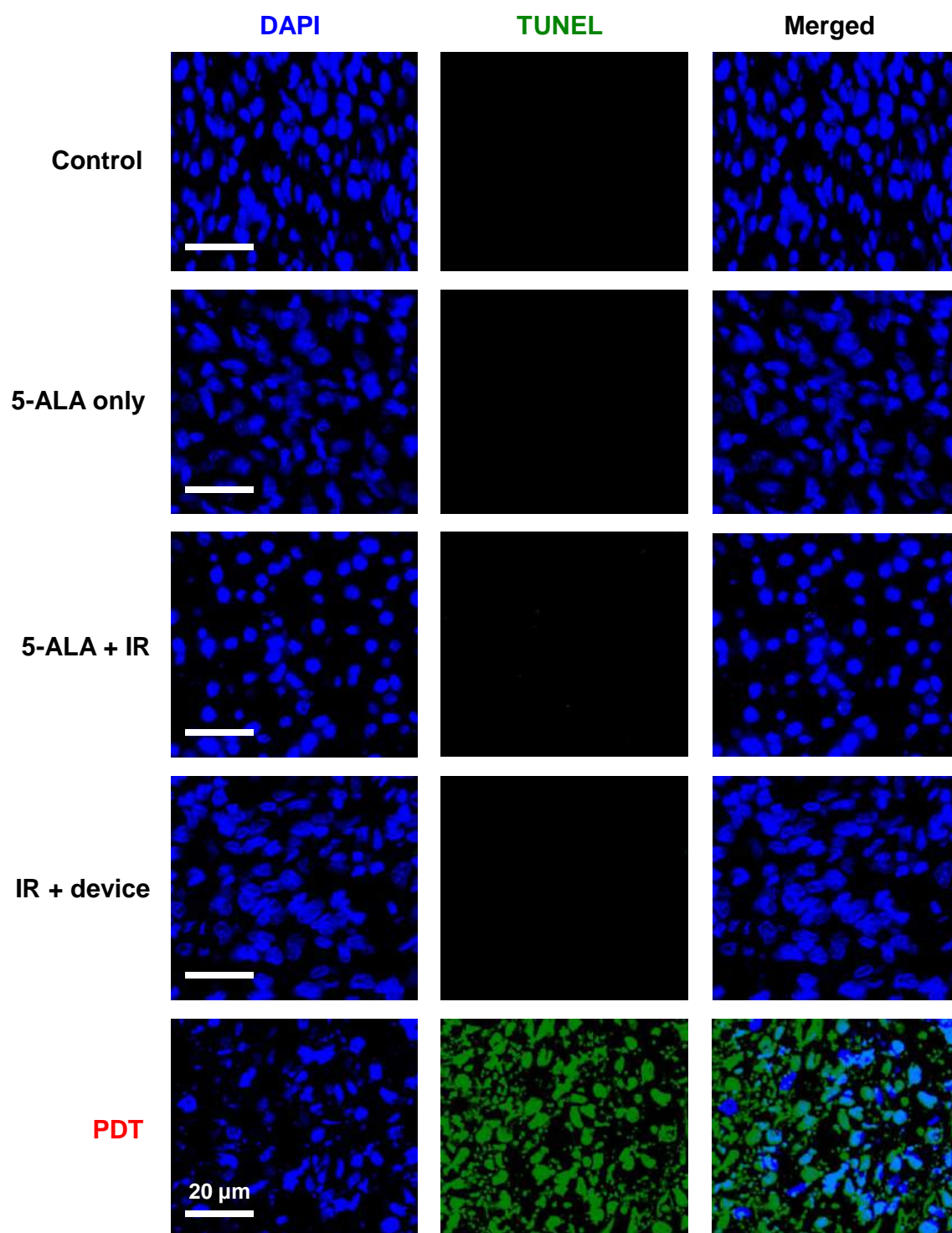


Figure S2. Histopathological images of tumor sections after PDT for different groups. DAPI (blue) indicates cell nuclei and TUNEL (green) indicates cell apoptosis.

Figure S3

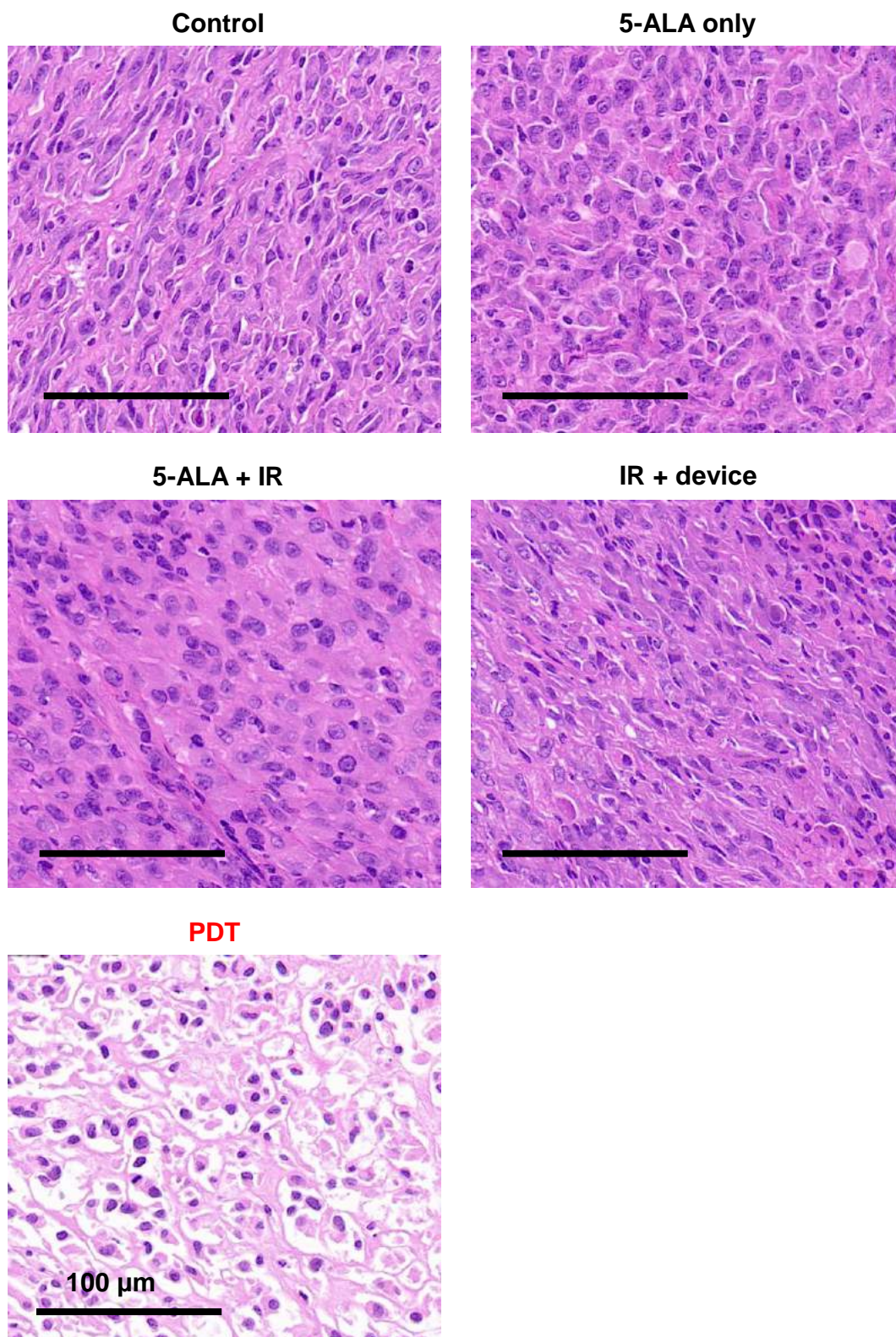


Figure S3. Histopathological images of tumor sections taken from mice after different treatments by H&E staining.

Figure S4

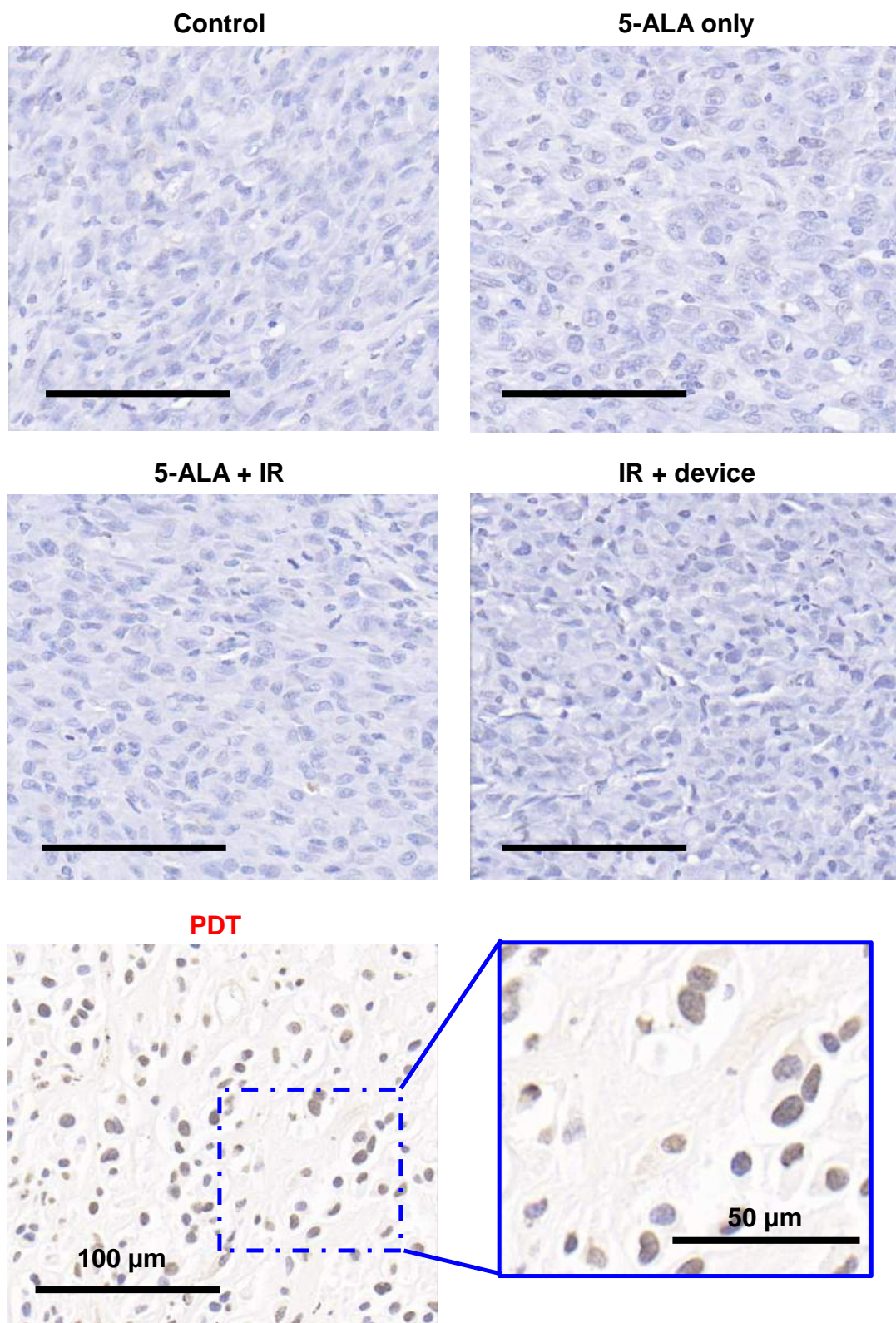


Figure S4. Histopathological images of tumor sections taken from mice after different treatments by DAB TUNEL staining.

Figure S5

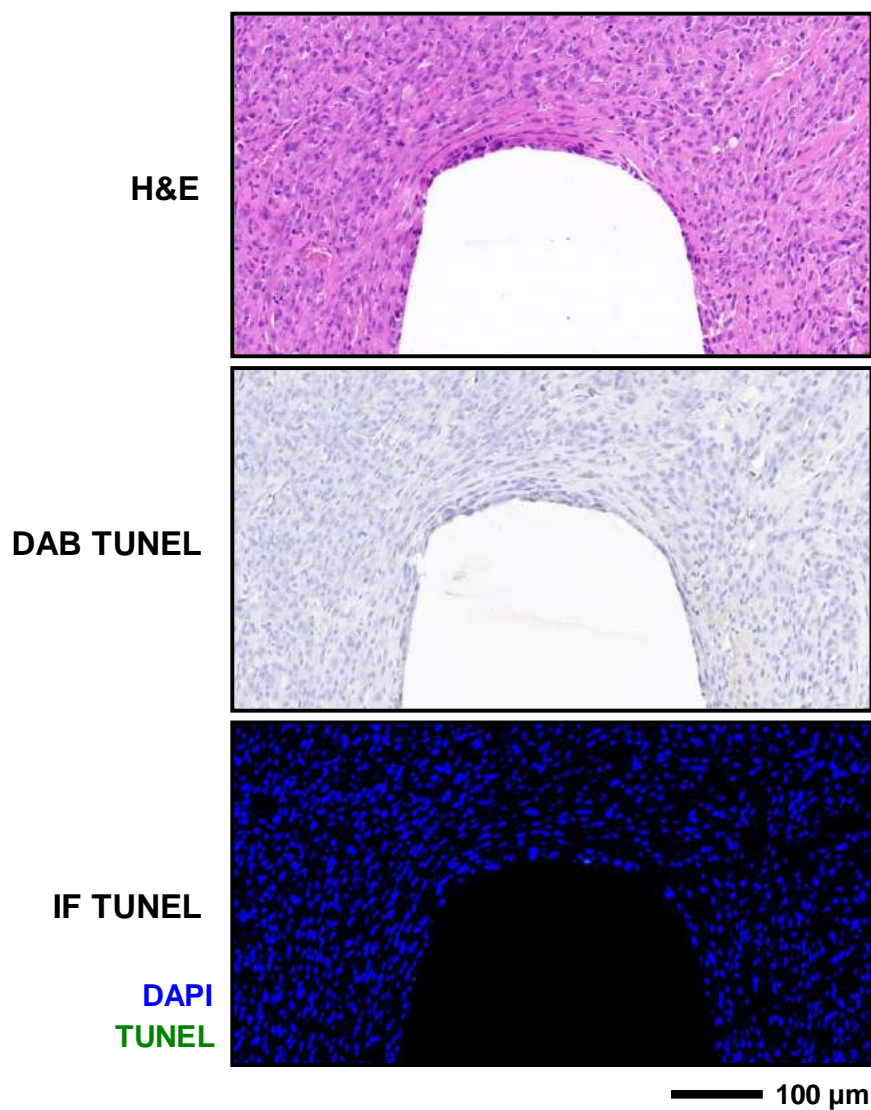


Figure S5. Histopathological images of tumor sections taken from a mouse in the control group near the waveguide region, by H&E, DAB TUNEL and IF TUNEL stainings.

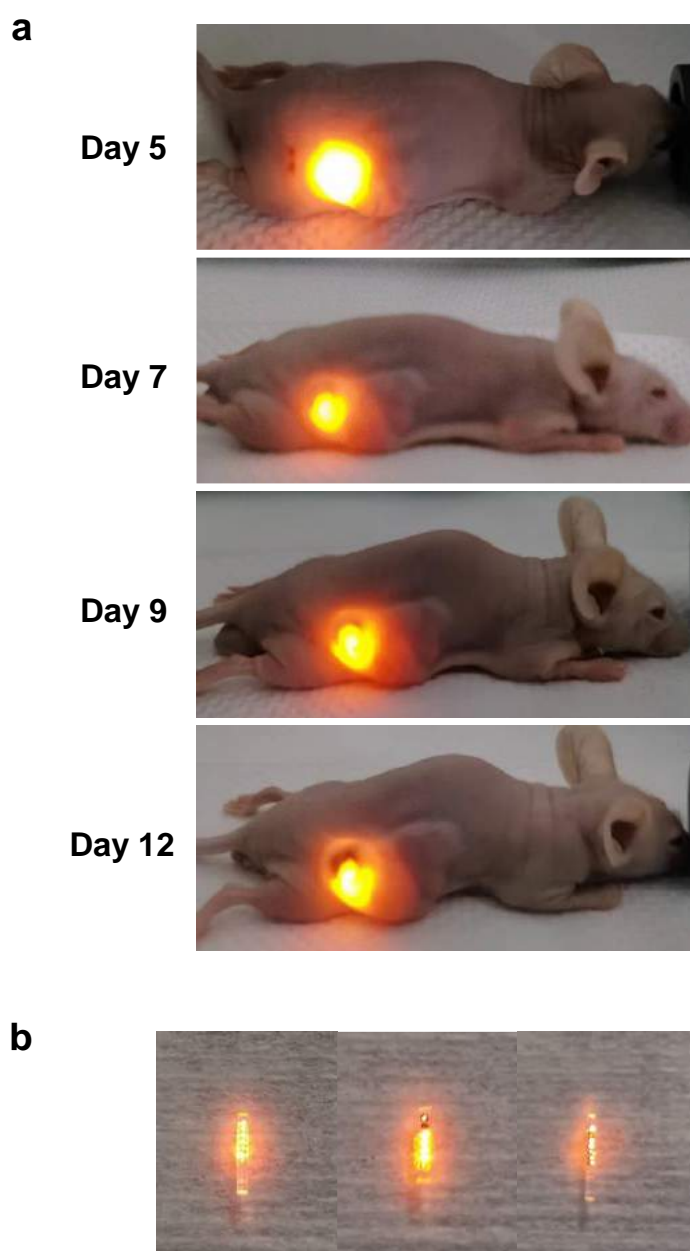
Figure S6

Figure S6. (a) Photos illustrating the emissions from the implanted waveguide excited by an external IR laser source, on day 5, 7, 9 and 12 post implantation. (b) These waveguides maintain their upconversion emissions after retrieved from tumors 18 days post implantation.

Table S1

	Waveguide (NOA 65)	Tissue (tumor)
refractive index (810 nm)	1.524	1.36
refractive index (630 nm)	1.524	1.36
absorption coefficient (810 nm)	10^{-5} mm^{-1}	0.01 mm^{-1}
absorption coefficient (630 nm)	10^{-5} mm^{-1}	0.025 mm^{-1}
scattering coefficient (810 nm)		20 mm^{-1}
anisotropy coefficient (810 nm)		0.95
scattering coefficient (630 nm)		30 mm^{-1}
anisotropy coefficient (630 nm)		0.95

Table S1. Parameters used in optical simulations.

Table S2

	Skin	Tissue (tumor)
refractive index (810 nm)	1.36	1.36
absorption coefficient (810 nm)	0.05 mm ⁻¹	0.01 mm ⁻¹
scattering coefficient (810 nm)	30 mm ⁻¹	20 mm ⁻¹
anisotropy coefficient (810 nm)	0.95	0.95
density	1109 kg/m ³	1090 kg/m ³
heat conductivity coefficient	0.37 W/(m K)	0.49 W/(m K)
heat capacity at constant pressure	3391 J/(kg K)	3421 J/(kg K)
blood perfusion rate	5 × 10 ⁻⁴ s ⁻¹	10 ⁻³ s ⁻¹
metabolic heat source	500 W/m ³	500 W/m ³

Table S2. Properties of tissue in photothermal simulation.

Table S3

arterial blood temperature	37 °C
blood density	1000 kg/m ³
specific heat capacity of blood	4000 J/(kg K)
surface irradiance rate	0.98
heat convection coefficient	5 W/(m ² K)

Table S3. Other parameters in photothermal simulation.